Intraoperative spectral domain optical coherence tomography for vitreoretinal surgery

Yuankai K. Tao,[1,*] Justis P. Ehlers,[2] Cynthia A. Toth,[2,1] and Joseph A. Izatt[1,2]

[1]*Department of Biomedical Engineering, Duke University, 136 Hudson Hall, Durham, North Carolina 27708, USA*

[2]*Department of Ophthalmology, Duke University Medical Center, DUMC 3802, Durham, North Carolina 27710, USA*

**Corresponding author: yt13@duke.edu*

Received July 14, 2010; accepted August 9, 2010;
posted September 2, 2010 (Doc. ID 131589); published October 7, 2010

We demonstrate *in vivo* human retinal imaging using an intraoperative microscope-mounted optical coherence tomography system (MMOCT). Our optomechanical design adapts an Oculus Binocular Indirect Ophthalmo Microscope (BIOM3), suspended from a Leica ophthalmic surgical microscope, with spectral domain optical coherence tomography (SD-OCT) scanning and relay optics. The MMOCT enables wide-field noncontact real-time cross-sectional imaging of retinal structure, allowing for SD-OCT augmented intrasurgical microscopy for intraocular visualization. We experimentally quantify the axial and lateral resolution of the MMOCT and demonstrate fundus imaging at a 20 Hz frame rate.

OCIS codes: 170.4460, 170.4470, 170.4500, 170.4580, 170.4730.

Surgical visualization has changed drastically since its inception, incorporating larger, more advanced optics toward increasing illumination and field of view (FOV). However, the limiting factor in vitreoretinal surgery remains the ability to distinguish between tissues with subtle contrast and to judge the location of an object relative to other retinal substructures [1]. Furthermore, increased illumination to supplement poor visualization is also limited by the risks of photochemical toxicity at the retina [2]. Finally, inherent issues in visualizing thin translucent tissues require the use of stains such as Indocyanine Green, which is toxic to the retinal pigment epithelium [3].

Spectral domain optical coherence tomography (SD-OCT) has demonstrated strong clinical success in retinal imaging, enabling high-resolution, motion-artifact-free cross-sectional imaging and rapid accumulation of volumetric macular datasets [4]. Current generation SD-OCT systems achieve <5 μm axial resolutions in tissue, and have been used to obtain high-resolution datasets from patients with neovascular age-related macular degeneration (AMD), high-risk drusen, and geographic atrophy [5].

Preoperative diagnostic imaging using current generation SD-OCT systems has demonstrated the ability to provide volumetric datasets of pathologic areas that are otherwise barely visible. OCT is uniquely suited for vitreoretinal surgery where multiple layers of the retinal structure are readily accessible and where high-resolution cross-sectional viewing would immediately have an impact on surgery. Real-time cross-sectional OCT imaging would provide critical information relevant to the location and deformation of structures that may shift during surgery. Combined OCT and surgical microscopy has previously been demonstrated for intraoperative examination of the anterior segment [6]. Here, we demonstrate *in vivo* human fundus imaging using an intraoperative microscope-mounted optical coherence tomography system (MMOCT). Our optomechanical design adapts an Oculus Binocular Indirect Ophthalmo Microscope (BIOM3), suspended from a Leica ophthalmic surgical microscope, with SD-OCT scanning and relay optics. The MMOCT enables wide-field, noncontact, real-time cross-sectional imaging of retinal structure, allowing for SD-OCT augmented intrasurgical microscopy for intraocular visualization.

The MMOCT was optically designed to work in conjunction with the optical path of an Oculus BIOM3 suspended from a Leica ophthalmic surgical microscope. The surgical microscope is designed to image through a BIOM3 adapter for wide-field indirect ophthalmoscopy during vitreoretinal surgery. The BIOM3 optically delivers an inverted wide-angle (120°) view of the retina to the image plane of the surgical microscope by the use of a high-power noncontact lens (90 D) and low-power reduction lens (*f*/200). When positioned adjacent to the objective lens of the surgical microscope, the BIOM3 creates a high-magnification optical telescope that relays a large FOV image of the fundus to the viewport of the surgical microscope.

The intraoperative MMOCT was implemented as an attachment to a Leica M841 ophthalmic surgical microscope with a BIOM3 attachment (Fig. 1). A superluminescent diode, with a center wavelength of 840 nm and a bandwidth of 49 nm, was used as the illumination source. The MMOCT sample arm included two-axis galvanometer scanners (G_x, G_y), a 12.5× beam expander (f_1, f_2), and relay optics (D, f_{Obj}, f_{Red}) to scan the SD-OCT beam, through the BIOM3 noncontact wide-field lens, across a 12 mm FOV on the retina of the patient. The system was designed to magnify the scanning SD-OCT beam diameter to accommodate for the demagnification introduced by the BIOM3 to preserve lateral resolution, and the scan pivot was optically relayed to the iris plane of the patient to ensure maximum FOV. The SD-OCT beam was designed to be folded into the optical path of the surgical microscope by using a dichroic mirror positioned in the infinity space of the surgical microscope, between the objective lens (Fig. 1—orange box) and the beam splitter and imaging optics of the microscope view ports (Fig. 1—green path). The position of this fold mirror was chosen to minimize the optical footprint under the BIOM3 adapter to avoid contact with the patient. Here, sharing the objective, reduction, and wide-field noncontact lenses (Fig. 1—orange and black

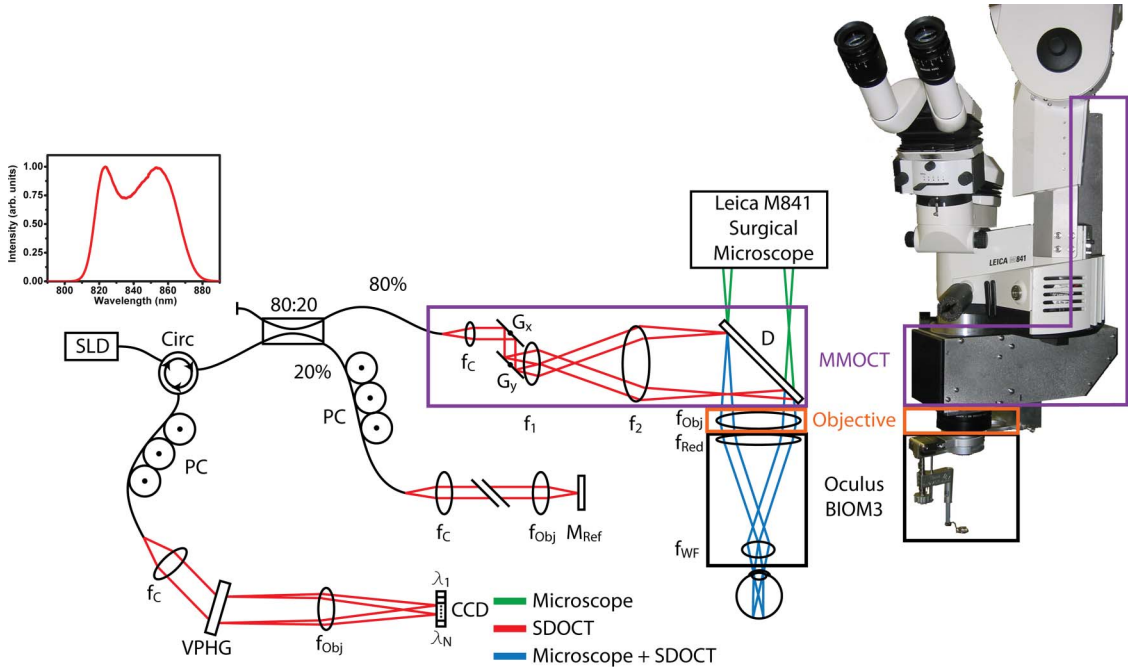

Fig. 1. (Color online) Optical schematic and photograph of the MMOCT showing surgical microscope (green), SD-OCT (red), and shared (blue) optical paths. The sample-arm optics of the MMOCT (purple box) consists of galvanometer scanners, a relay telescope, a dichroic beam splitter, and focusing optics from the surgical microscope, including a microscope objective (orange box) and reduction and wide-field ophthalmic lenses (black box). CCD, linear CCD array; D, dichroic mirror; f, focal length of collimating, relay, and focusing elements; G, galvanometer; M, mirror; PC, polarization controller; VPHG, grating.

boxes) between the OCT and microscope optical paths allowed for a common focal plane between the two modalities (Fig. 1—blue path), which could be adjusted together by changing the axial position of the wide-field lens. This particular MMOCT design offers advantages over imaging using a hand-held OCT system during surgery by providing a stable imaging arm; however, since the OCT is relayed through the microscope objective, reduction, and high-powered (90 D) wide-field noncontact lenses, the lateral resolution and FOV of the OCT are limited by the performance of these optics at 840 nm. Interferometric signals were captured using a 1024 pixel subset of a 2048 pixel line-scan CCD camera (SM2CL 2014-e2v, Ltd.). Custom software (Bioptigen, Inc.) performed real-time data acquisition, processing, archiving, and display. Using 700 μW of illumination power at the sample, the signal-to-noise ratio (SNR) measured near DC from an ideal reflector was 112 dB with an axial resolution of 6.51 μm in air, 6 dB falloff at 1.45 mm, and total axial range of 2.24 mm.

Optical design simulations (ZEMAX) of the MMOCT, using a Pomerantzef model eye [7] as the sample, vendor-provided lens models for the MMOCT relay optics (Fig. 1—purple box), and paraxial approximations for the microscope objective (Fig. 1—orange box) and BIOM3 lenses (Fig. 1—black box), yielded theoretical FWHM spot sizes of 10 μm over a 12 mm FOV. The lateral resolution was then evaluated experimentally by measuring the optical transfer function (OTF) and subsequently calculating the point spread function (PSF) at the focal plane [Figs. 2(a)–2(c)]. The OTF was measured experimentally by acquiring a series of images of a USAF 1951 test chart, positioned at the focal plane of a model eye, consisting of a 40 D focusing objective and an adjustable iris. The lateral OTF cross-section was then calculated using the normalized contrast of each group of elements [Fig. 2(a)], and the respective PSF cross section was calculated from the Fourier transform of the OTF [Fig. 2(b)]. Finally, lateral cross sections of the measured lateral PSF function were compared with theoretical

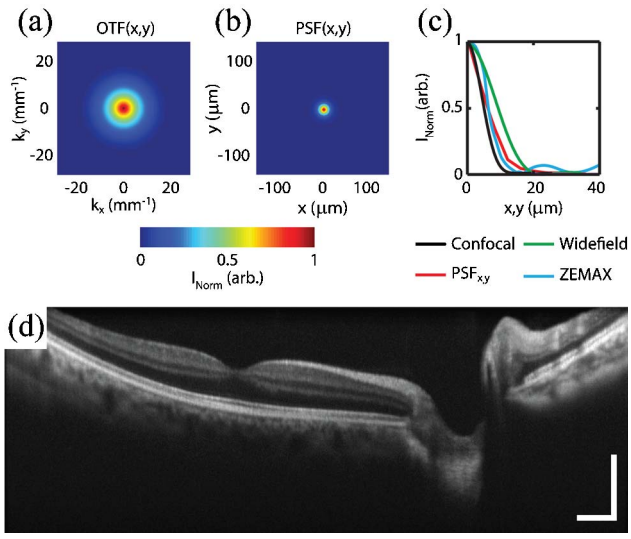

Fig. 2. (Color online) Resolution of MMOCT. Focal plane cross sections of the lateral (a) OTF and (b) PSF, calculated from the Fourier transform of the OTF. (c) Lateral PSF cross section compared with theoretical values for confocal and wide-field imaging systems, and ZEMAX simulations. (d) Ten coregistered and averaged image excerpts from a video of 8 mm × 1.75 mm (lateral × depth) *B*-scans of *in vivo* human macula (Media 1). Images were acquired with 1024 × 1024 pixels (lateral × spectral) at a frame rate of 20 Hz. Illumination power, 700 μW; scale bar, 2°.

values for confocal and wide-field imaging systems, as well as values simulated using ZEMAX [Fig. 2(c)]. For an illumination beam diameter of 2.5 mm at the pupil, these PSFs showed FWHM resolutions of 16, 12, 34, and 16 μm for the measured, theoretical confocal, theoretical wide-field, and ZEMAX simulated values, respectively. The theoretical lateral PSF at the focal plane of a confocal system is described by $I(v) = [2J_1(v)/v]^4$ [8]. Here, $v = (2\pi/\lambda)r\sin(\alpha)$, where r is the radial position and α is the half-angle subtended by the objective. The measured lateral PSF cross sections were well correlated with theoretical and simulated values and demonstrated a confocal resolution improvement when compared with the theoretical PSF cross section for wide-field imaging. These theoretical lateral resolution limits, however, will ultimately be dominated by the confocal focused spot size and aberrations present in the eye.

In vivo human fundus was imaged using the MMOCT with 700 μW illumination power at the pupil to demonstrate image quality over an 8 mm FOV [Fig. 2(d)] (Media 1). Degradation of lateral resolution at the edges of the image may be attributed to beam-quality nonuniformity associated with scanning across the aspheric high-powered (90 D) wide-field noncontact ophthalmic lens. Human images were acquired in accordance with a protocol approved by the Duke University Health System Institutional Review Board. All subjects were imaged in the supine position, without pupil dilation or any contact with the eye. MMOCT alignment and aiming was accomplished using the foot-pedal-controlled articulating arm of the surgical microscope, simulating intraoperative operation. All images were acquired with 1024×1024 pixels (lateral $\times$ spectral) at a 20 kHz line rate for continuous imaging at a 20 Hz frame rate. Ten of these frames were then coregistered and averaged for improved SNR and speckle reduction in postprocessing.

MMOCT images of surgical manipulations, performed in cadaveric porcine eyes, were acquired over a 6 mm $\times$ 6 mm FOV with 500 *B*-scans, sampled with 1024×500 pixels (spectral $\times$ lateral) at a 20 kHz line rate (Fig. 3). The surgical procedure was performed by viewing the retina through the surgical microscope, simulating vitreoretinal surgery conditions, with concurrent acquisition of MMOCT volumes. The porcine retina was illuminated using a fiber-optic light pipe and manipulated using vitreoretinal surgical forceps. The retina and surgical instruments were visible through conventional viewing through the pupil via the microscope. The volumetric rendering [Fig. 3(a)] (Media 2) and summed-voxel projection (SVP) [Fig. 3(b)] allow for MMOCT visualization of both the instrument (red arrow) and a piece of glial tissue extruding from the optic nerve (green arrow). The volume rendering shows that the tissue below the forceps is obscured by shadows [Fig. 3(a)] (Media 2), and most of the instrument is not visible because the polished metal edges of the forceps specularly reflect the OCT light outside of the collection aperture of the MMOCT. However, the structure and orientation of the forceps can clearly be visualized on the SVP [Fig. 3(b)]. MMOCT visualization of surgical tools may be enhanced by artificially creating scattering surfaces, such as by roughening the flat faces of instruments. Sequential *B*-scans were coregistered to remove interframe bulk motion artifacts and the dataset was displayed as a volumetric rendering using Amira (Visage Imaging, Inc.) in postprocessing.

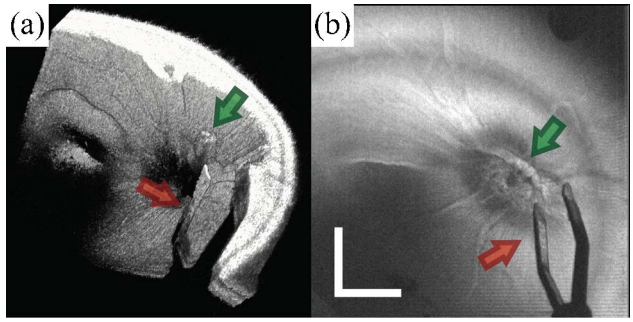

Fig. 3. (Color online) MMOCT of surgical instrument (forceps) over the optic nerve in cadaveric porcine eye. The surgical procedure was performed by viewing through the surgical microscope with concurrent acquisition of MMOCT volumes. A 6 mm $\times$ 6 mm volumetric dataset was acquired with 500 *B*-scans, sampled with 1024×500 pixels (spectral $\times$ lateral) at a 20 kHz line rate. (a) Volumetric rendering (Media 2) and (b) SVP show both the instrument (red arrow) and a piece of glial tissue extruding from the optic nerve (green arrow). Illumination power, 700 μW; scale bar, 3°.

We have demonstrated MMOCT as a method for combining SD-OCT with a Leica ophthalmic surgical microscope. The optomechanical design of the system allowed for a combination of SD-OCT and microscope optical paths that maintained both the large FOV of the surgical microscope and high lateral and axial resolution of standard ophthalmic SD-OCT. Furthermore, the MMOCT provides a more stable imaging platform over handheld implementations of ophthalmic SD-OCT, and the system shares a common focus with the surgical microscope, which allows for simple multimodal imaging of supine patients. Finally, we presented video-rate acquisition of cross-sectional images of retinal structure, demonstrating the potential for SD-OCT augmented intrasurgical microscopy for intraocular visualization.

The authors acknowledge the contributions of Ramiro Maldonado from the Department of Ophthalmology, Duke University Medical Center. This research was supported by grant EY-019411 from the National Institutes of Health (NIH).

References

1. S. R. Virata, J. A. Kylstra, and H. T. Singh, Retina **19**, 287 (1999).
2. S. Charles, Retina **28**, 1 (2008).
3. F. Ando, K. Sasano, N. Ohba, H. Hirose, and O. Yasui, Am. J. Ophthalmol. **137**, 609 (2004).
4. N. A. Nassif, B. Cense, B. H. Park, M. C. Pierce, S. H. Yun, B. E. Bouma, G. J. Tearney, T. C. Chen, and J. F. de Boer, Opt. Express **12**, 367 (2004).
5. M. Stopa, B. A. Bower, E. Davies, J. A. Izatt, and C. A. Toth, Retina **28**, 298 (2008).
6. G. Geerling, M. Muller, C. Winter, H. Hoerauf, S. Oelckers, H. Laqua, and R. Birngruber, Arch. Ophthalmol. **123**, 253 (2005).
7. O. Pomerantzeff, H. Fish, J. Govignon, and C. L. Schepens, Ann. Ophthalmol. **3**, 815 (1971).
8. T. Wilson, *Confocal Microscopy* (Academic, 1990).